

Two-dimensionality of metallic surface conduction in $\text{Co}_3\text{Sn}_2\text{S}_2$ thin films

Junya Ikeda¹, Kohei Fujiwara ^{1✉}, Junichi Shiogai ¹, Takeshi Seki^{1,2}, Kentaro Nomura^{1,2}, Koki Takanashi^{1,2,3} & Atsushi Tsukazaki ^{1,2,3}

Two-dimensional (2D) surface of the topological materials is an attractive channel for the electrical conduction reflecting the linearly-dispersive electronic bands. Thickness-dependent sheet conductance measurement is a reliable method to evaluate the 2D and three-dimensional (3D) electrical conducting channel separately but has rarely been applied for Weyl semimetals. By applying this method to thin films of a Weyl semimetal $\text{Co}_3\text{Sn}_2\text{S}_2$, here we show that the 2D conducting channel clearly emerges under the ferromagnetic phase, indicating a formation of the Fermi arcs projected from Weyl nodes. Comparison between 3D conductivity and 2D conductance provides the effective thickness of the surface conducting region being estimated to be approximately 20 nm, which would reflect the Weyl feature of electronic bands of the $\text{Co}_3\text{Sn}_2\text{S}_2$. The emergent surface conduction will provide a pathway to activate quantum and spintronic transport features stemming from a Weyl node in thin-film-based devices.

¹Institute for Materials Research, Tohoku University, Sendai, Japan. ²Center for Spintronics Research Network (CSRN), Tohoku University, Sendai, Japan. ³Center for Science and Innovation in Spintronics (CSIS), Core Research Cluster, Tohoku University, Sendai, Japan. ✉email: kfujiwara@imr.tohoku.ac.jp

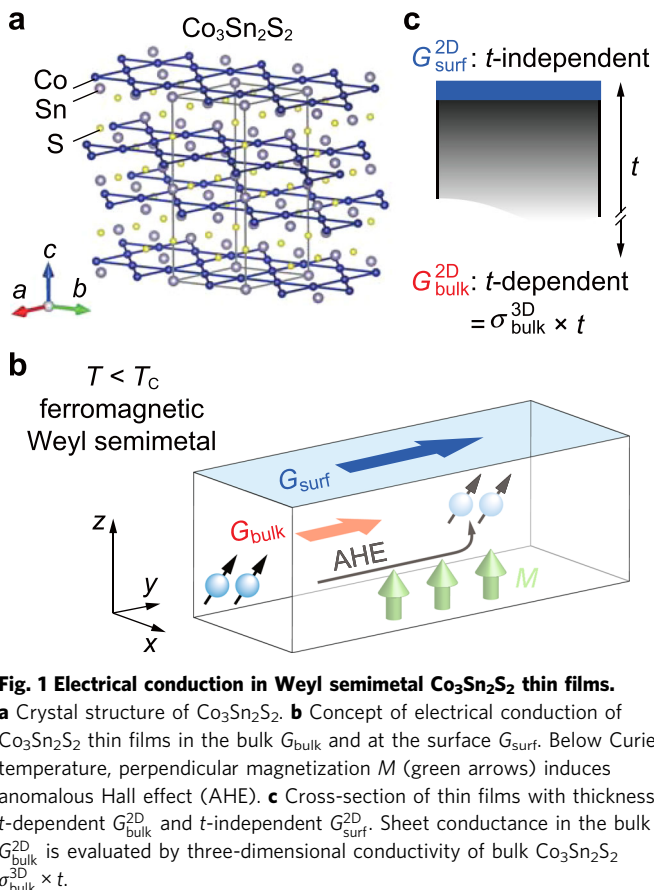
The surface of the films forms interface with substrate or capping layer, which usually plays an active role for the electrical conduction in addition to the bulk region. Various origins for the interface conduction in trivial semiconductors have been explored as charge discontinuity at oxide interface¹, charge transfer², dipoles effect³, and electric polarization effect^{4,5}. The effective thickness of the two-dimensional (2D) conducting channel is basically dominated by charge accumulation based on Poisson equation. Besides these interface effects, the emergent topological materials hold intrinsic surface conducting channels that are a Dirac surface state in three-dimensional (3D) topological insulator (TI)⁶ and Fermi arc in Dirac and Weyl semimetals^{7,8}. The surface conduction in the topological materials exhibits the intriguing features of linearly-dispersive electronic bands such as spin-momentum locking^{9,10}, quantum anomalous Hall effect^{11,12}, and magnetoresistance oscillation at the Weyl orbits^{13,14}. As another important feature, the surface states of TIs suddenly disappear by hybridization between two surfaces of top and bottom in ultrathin films. While the dominant factor of the penetration function along thickness direction has been experimentally^{15,16} and theoretically¹⁷ investigated, the critical thickness for 3D-TIs is about 5 nm for Bi₂Se₃ (ref. ¹⁵) and 2 nm for Bi₂Te₃ (ref. ¹⁶). However, surface conduction in Weyl semimetal (WSM) has been rarely explored in thin films. Recently, a Co-kagome magnet of Co₃Sn₂S₂, crystal structure of which is shown in Fig. 1a, has been extensively investigated as a Dirac semimetal (DSM) at paramagnetic phase and a WSM at ferromagnetic phase^{18–23}. Among proposed Weyl semimetals, Co₃Sn₂S₂ is an ideal material for the electrical detection of surface conduction because (i) the Weyl points are very close to the Fermi level¹⁸, (ii) the linearly-dispersive bands dominantly contribute to density-of-states at the Fermi level¹⁸, (iii) the Curie temperature (T_C) of ~180 K is relatively high as a kagome-lattice

ferromagnet with electrical conduction. Large anomalous Hall conductivity has been focused with perpendicular magnetic anisotropy owing to large contribution of Berry curvature in the Weyl nodes¹⁸. By tilting the symmetric line of the two Weyl nodes from z -axis, surface Fermi arc has been observed by spectroscopies^{21–23}. The contribution of the projected Weyl nodes would be detected in electrical conduction for ultrathin films with suppressed bulk conduction though it has not been apparently obtained in bulk Co₃Sn₂S₂.

The electrical conduction in thin films at zero magnetic field is generally expected to follow the Ohm's law based on the 3D uniform conductivity σ_{xx} ($\Omega^{-1}\text{cm}^{-1}$) in whole region of the film; $G = \frac{I}{V} = \sigma_{xx} \frac{tW}{L}$, where G is the conductance of the sample, I current, V applied voltage, W width, L length, and t thickness of the channel. The sheet conductance is experimentally calculated by $G_s = \frac{I}{VW} = t\sigma_{xx}$. When the surface or interface contributes to the electrical conduction in the films, the sheet conductance of the film G_{total}^{2D} sums up the t -dependent conductance in bulk region $G_{\text{bulk}} = t\sigma_{\text{bulk}}^{3D}$ and the t -independent 2D surface conductance G_{surf}^{2D} , $G_{\text{total}}^{2D} = t\sigma_{\text{bulk}}^{3D} + G_{\text{surf}}^{2D}$ as shown in Fig. 1b, c, where $\sigma_{\text{bulk}}^{3D}$ is the 3D conductivity of the bulk region. Experimentally, t dependence of the 2D sheet conductance G_{total}^{2D} can separately elucidate the conducting channel at 3D bulk and 2D surface when these contributions are comparable in thin films. However, it is often difficult to achieve the electrical conduction in the ultrathin layers because the island-like grains initially disconnect each other. This is so-called a dead layer at the interface, which is usually evaluated by the t -dependent conductance measurement. To accurately evaluate the bulk conductivity $\sigma_{\text{bulk}}^{3D}$ of the thin films, therefore, the t -dependent measurement is reliable with elimination of the additional conduction at the surface and/or with accurate thickness contributing conduction except for a dead layer. In this study, we applied this analysis to the Co₃Sn₂S₂ thin films to elucidate the dimensionality of the conducting channels at bulk and surface separately. The films holding WSM phase are intensively discussed in thickness 23–61 nm. The metallic conduction of the films at the WSM phase strongly relates to the superior surface conduction.

Results

Temperature dependence of electrical resistivity. Temperature dependent resistivity ρ_{xx} of two Co₃Sn₂S₂ films with thicknesses of 41 and 40 nm is shown in Fig. 2a with a reference ρ_{xx} of bulk crystal¹⁸. The two films are typical examples for 12 films with various thicknesses t (23–61 nm), prepared by radio-frequency sputtering (Methods section)^{24,25}. Atomic force microscopy observation detected comparable surface roughness values on SiO_x cap layers of the two films (Supplementary Fig. 1). All three traces in Fig. 2a clearly present a kink ~180 K coming from the ferromagnetic transition, corresponding to a phase transition from DSM at $T > T_C$ to WSM at $T < T_C$. This feature is in fact detected in magnetization and anomalous Hall conductivity^{24,25}. Since metallic conduction is more pronounced in the WSM phase, here we define the residual resistivity ratio (RRR = $\rho_{xx}(T = 300\text{ K})/\rho_{xx}(T = 2\text{ K})$) to characterize the metallicity of the films. This RRR is a good measure to classify the films into two groups while the structural qualities of these films are comparable in the inspection by x-ray diffraction²⁵. In Fig. 2b, the RRR for all the films measured in this study is summarized with the bulk value¹⁸ to classify the films into Groups A (blue) and B (red), in which the border for classification is RRR ~ 4. Typical ρ_{xx} values for the film #1 of Group A and the film #2 of Group B with comparable $t \sim 40$ nm represent large and small RRR in Fig. 2a, respectively. In comparison with the reference ρ_{xx} of bulk crystal with large RRR ~ 8.5, ρ_{xx} of #1 at low temperature is comparable



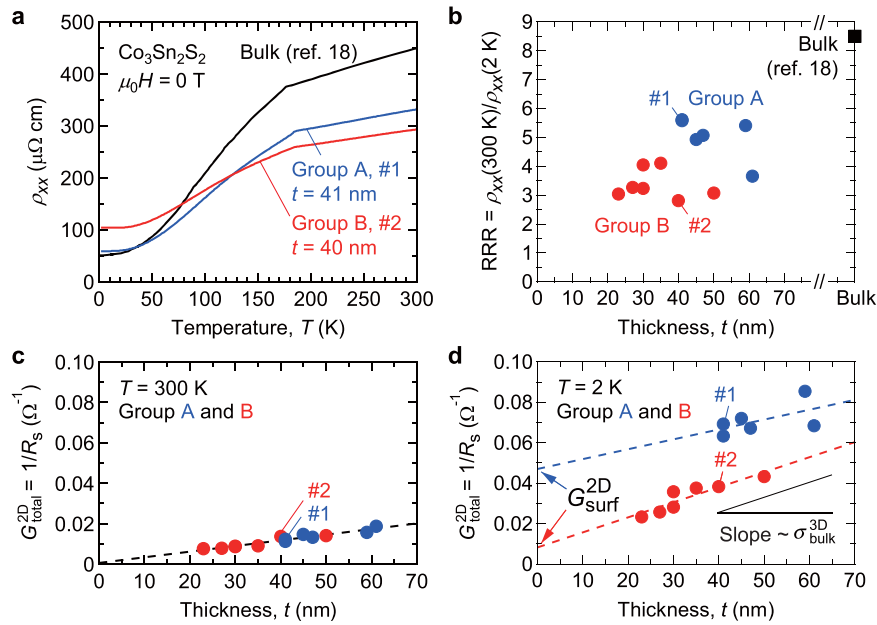


Fig. 2 Temperature T and thickness t dependence of electrical conduction in $\text{Co}_3\text{Sn}_2\text{S}_2$ thin films. **a** T dependence of resistivity ρ_{xx} , for a reference of bulk (black curve from Liu et al.¹⁸), film #1 (blue curve; $t = 41$ nm) from Group A, and film #2 (red curve; $t = 40$ nm) from Group B. **b** Residual resistivity ratio RRR for the films as a function of thickness, which guided to categorize the films to Group A and B by the criteria at roughly RRR = 4. The bulk value of RRR = 8.5 (Liu et al.¹⁸) is included for comparison. **c, d** To detect the t -independent conductance, sheet conductance $G_{\text{total}}^{2\text{D}}$ for various thickness films at $T = 300$ K and 2 K are plotted, respectively. The slope corresponds to three-dimensional conductivity $\sigma_{\text{bulk}}^{3\text{D}}$. The detection of intercept in **d** indicates the emergence of t -independent two-dimensional surface conductance $G_{\text{surf}}^{2\text{D}}$. The experimental data in **a** and **d** are replotted from Ikeda et al.²⁵.

to that of the bulk but the ρ_{xx} of both the films at high temperature is largely different.

Detection of 2D surface conductance in WSM phase. Thickness t dependence of sheet conductance ($G_s = 1/R_s$, where R_s is sheet resistance) at $T = 300$ K and 2 K is plotted as a function of t in Fig. 2c, d, respectively. In DSM phase at 300 K, the sheet conductance linearly depends on t . In addition, the intercept of the fitting line is close to the origin, holding a dead layer thickness of roughly 1 nm. This linear trend and the small intercept, as well as the negligibly small strain as revealed by transmission electron microscopy analysis (Supplementary Fig. 2), support the validity of this t -dependent analysis based on the uniform crystalline quality of the films. The slope in this plot corresponds to the conductivity of the bulk $\sigma_{\text{bulk}}^{3\text{D}}$ as a usually discussed fundamental physical parameter. In contrast, the intercept of the fitting line at $T = 2$ K in Fig. 2d apparently reveals the emergence of t -independent 2D conducting channel at extrapolated $t = 0$ nm, corresponding to the 2D surface conductance $G_{\text{surf}}^{2\text{D}}$. This dramatic variation of the intercept in the fitting line from 300 K to 2 K (also see Supplementary Fig. 3) strongly indicates the unique surface transport of the Fermi arc states, relating on the spontaneous symmetry breaking and Fermi energy. The Fermi energy in the non-magnetic phase is far from the Dirac point²⁶, being the maximum density of state that relates on the Stoner criterion for the ferromagnetism in $\text{Co}_3\text{Sn}_2\text{S}_2$. By contrast, the Fermi energy becomes rather close to the Weyl nodes below T_C (refs. 18,26), which is the origin for the distinct appearance of the surface state in only WSM phase.

Evaluation of 2D and 3D conducting channel separately. At the various temperatures, t -dependent analysis was carried out to elucidate the $\sigma_{\text{bulk}}^{3\text{D}}$ and $G_{\text{surf}}^{2\text{D}}$. In addition, the total conductivity σ_{xx} of the films is calculated by conventional scheme $\sigma_{xx} = \frac{\rho_{xx}}{(\rho_{xx}^2 + \rho_{yx}^2)}$, where ρ_{xx} is resistivity and ρ_{yx} Hall resistivity for

estimation under the assumption of uniform conduction in whole region. Figure 3a, b shows the σ_{xx} (black line) for the films #1 and #2 and the analyzed $\sigma_{\text{bulk}}^{3\text{D}}$ (red circles) as discussed in Fig. 2c, d for the Group A and B, respectively. Above $T_C \sim 180$ K, the analyzed $\sigma_{\text{bulk}}^{3\text{D}}$ matches well with the σ_{xx} , meaning that the analysis is valid for estimation of bulk conductivity for DSM phase. In WSM phase below T_C , the $\sigma_{\text{bulk}}^{3\text{D}}$ (red closed circles) gradually increases with decreasing temperature, implying the suppression of spin disorder scattering and/or magnon-phonon scattering^{19,27–29} as like half-metallic ferromagnetic materials. Moreover, the σ_{xx} for #1 (black line) represents superior metallic behavior at low temperature, the value of which is much higher than the $\sigma_{\text{bulk}}^{3\text{D}}$. This deviation indicates the contribution of additional conducting channel to that of the t -dependent bulk, which is the t -independent surface conduction (blue region). By contrast, in Fig. 3b, the σ_{xx} for #2 (black line) is comparable to the $\sigma_{\text{bulk}}^{3\text{D}}$ (red open circles) for Group B. Considering the comparable $\sigma_{\text{bulk}}^{3\text{D}}$ for Group A and B, the superior metallic conduction of σ_{xx} for #1 is mainly driven by the surface conduction.

Effective thickness of 2D surface conducting channel. The analyzed $G_{\text{surf}}^{2\text{D}}$ for Group A and B is plotted as a function of temperature in Fig. 4a. The $G_{\text{surf}}^{2\text{D}}$ increases with decreasing temperature in WSM phase for both Groups. The steep increase of $G_{\text{surf}}^{2\text{D}}$ for Group A induces the large σ_{xx} of the films in Group A. Judging from the consistent trend between the σ_{xx} shown in Fig. 3 and the $G_{\text{surf}}^{2\text{D}}$ in Fig. 4a, the difference between the observed σ_{xx} (black line) and the analyzed $\sigma_{\text{bulk}}^{3\text{D}}$ (red circles) in Fig. 3; $\sigma_{xx} - \sigma_{\text{bulk}}^{3\text{D}} = \sigma_{\text{surf}}^{3\text{D}}$, corresponds to the contribution of 2D $G_{\text{surf}}^{2\text{D}}$. Considering the units of $\sigma_{\text{surf}}^{3\text{D}}$ and $G_{\text{surf}}^{2\text{D}}$, we estimate the effective thickness of the surface conduction $t_{\text{surf}}^{\text{eff}}$ by a following equation $\sigma_{\text{surf}}^{3\text{D}} \times t_{\text{surf}}^{\text{eff}} \times 2 = G_{\text{surf}}^{2\text{D}}$ where the factor of 2 corresponds to two surfaces of the films. Although the error bar is large in Fig. 4b, the t -independent 2D conduction region is estimated to be roughly

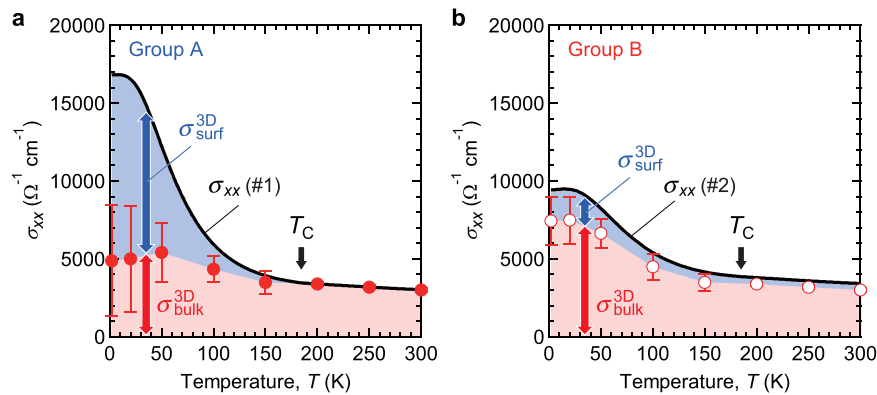


Fig. 3 Analyzed conductance for bulk and surface in $\text{Co}_3\text{Sn}_2\text{S}_2$ thin films. **a, b** The $\sigma_{\text{bulk}}^{3\text{D}}$ is estimated by the slope in t -dependent sheet conductance for Group A and B as shown in Fig. 2c, d. Temperature dependence of the analyzed $\sigma_{\text{bulk}}^{3\text{D}}$ is plotted with the obtained conductance data for the representative film #1 in A and #2 in B (black line). The deviation between the black line and $\sigma_{\text{bulk}}^{3\text{D}}$ corresponds to the contribution of electrical conduction at the surface $\sigma_{\text{surf}}^{3\text{D}}$. The error bars represent the standard deviations of the calculated $\sigma_{\text{bulk}}^{3\text{D}}$.

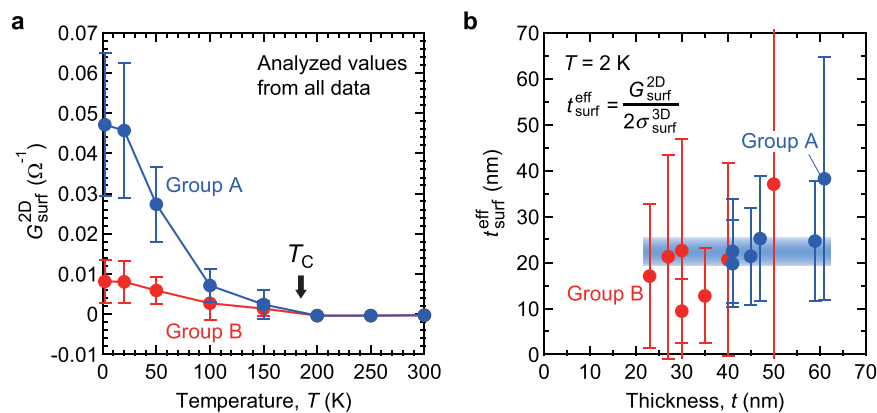


Fig. 4 Comparison of 2D conduction $G_{\text{surf}}^{2\text{D}}$ and averaged 3D thickness of the surface conducting channel. **a** Temperature dependence of the surface conduction $G_{\text{surf}}^{2\text{D}}$ by the analysis as shown in Fig. 2d for the data of Group A (blue) and B (red). **b** Under the assumption of uniform electrical conduction at the surface region, the effective thickness of surface conduction $t_{\text{surf}}^{\text{eff}}$ is calculated by $t_{\text{surf}}^{\text{eff}} = \frac{G_{\text{surf}}^{2\text{D}}}{2\sigma_{\text{surf}}^{3\text{D}}}$ at $T = 2$ K. The error bars represent the standard deviations of the calculated $G_{\text{surf}}^{2\text{D}}$ and $t_{\text{surf}}^{\text{eff}}$ in **a** and **b**, respectively.

20 nm constant against t -variation. This value is rather thicker than that of 3D-TI for example 5 nm of Bi_2Se_3 (ref. 15). The distribution of surface Fermi arc along z -direction may be related to the broadness of the projection of Weyl nodes with narrow gap¹⁷. Based on empirical facts that weakening of spin-orbit coupling tends to increase the critical thickness in 3D-TIs such as Bi_2Se_3 and Bi_2Te_3 (refs. 15–17), the weaker spin-orbit coupling of $\text{Co}_3\text{Sn}_2\text{S}_2$ composed of lighter elements may induce the weak confinement of surface state, resulting in the large effective thickness. While we here assume uniform $G_{\text{surf}}^{2\text{D}}$ to estimate the averaged effective thickness, the penetration function of the surface conduction region should be more carefully considered to be rapid decay along z -direction as like 3D-TIs^{17,30}. It will be important to clarify the correspondence between the estimated $t_{\text{surf}}^{\text{eff}}$ and the real-space distribution of the surface states. While the values of $\sigma_{\text{bulk}}^{3\text{D}}$ and $G_{\text{surf}}^{2\text{D}}$ are influenced by the defects in bulk and surface region, the $t_{\text{surf}}^{\text{eff}}$ is likely valid owing to the independent analysis for the estimation of bulk and surface contribution. In this study, apparent detection of the t -independent conductance reveals the possibility of surface Fermi arc conduction in the $\text{Co}_3\text{Sn}_2\text{S}_2$ thin films.

Discussion

Here we discuss the origin for the appearance of t -independent surface conduction in the films. The robust t -independent current

path is experimentally detected by the analysis of sheet conductance of the films. The thickness of the films is thick enough to form uniform crystalline structure and to hold a feature of WSM with large anomalous Hall conductivity²⁵. The top and bottom surfaces of the films form the interface with a capping layer of SiO_x and Al_2O_3 substrate, respectively. Such interface between oxide insulator and sulfide metal is likely to be basically inactive for the electrical conduction. Other extrinsic defect formation contributing to the metallic electrical conduction can be excluded. As intrinsic origins, the surface projected Fermi arc is possibly located at the inert interface. Moreover, the appearance of surface conduction below T_C should be noticeable to the Weyl nodes stemming from WSM phase. However, the origin for different values of RRR in two groups is not obvious from the structural quality. In fact, the analyzed value of $\sigma_{\text{bulk}}^{3\text{D}}$ for both group is comparable. The resultant $G_{\text{surf}}^{2\text{D}}$ originating from clear classification of Group A and B in Fig. 2d is mainly related to the difference of RRR. As shown in Fig. 2b, most of the films in Group A are roughly thicker than those in Group B, implying that 40 nm $\sim 2 \times t_{\text{surf}}^{\text{eff}}$ looks criteria for the large surface conduction. The surface conduction in the WSMs may be weakened by hybridization each other. Single crystalline bulk also presents large RRR (Liu et al.¹⁸), even though the electrical conduction is dominated by the G_{bulk} due to thick limit. To be consistent with the bulk results, the detected surface conduction is likely to shed light on the thin films with less contribution of bulk conduction.

In addition, the surface termination might be a plausible origin for holding different Fermi surface contributing to the electrical conduction^{7,21,22,31}, although determination of the surface termination of $\text{Co}_3\text{Sn}_2\text{S}_2$ thin film is difficult in the present sample structure. The superior metallic surface conduction in Group A may link to the rich surface Fermi arc by sulfur termination. On the sulfur terminated surface, the sulfur vacancies detected by tunneling spectroscopy might influence the 2D surface conduction via a local modification of the electronic states^{22,32}. By contrast, the less surface conduction in Group B may be terminated by Sn. The further studies on specific interface formation need to clarify the termination and contribution to the charge distribution.

Conclusions

Systematic thickness dependence of conductance reveals the emergence of t -independent 2D conducting channel in the $\text{Co}_3\text{Sn}_2\text{S}_2$ films under Weyl semimetal phase. Based on the analysis for two group films, superior metallic conduction at surface dominates the large RRR of the films. Origin for the appearance of 2D metallic conducting channel is likely the surface Fermi arc projected from Weyl nodes. Broad penetration of the 2D surface state comes from material specific parameters of Weyl semimetal $\text{Co}_3\text{Sn}_2\text{S}_2$ such as strength of spin-orbit coupling and gap size at Weyl point. The interface formation with the $\text{Co}_3\text{Sn}_2\text{S}_2$ will provide an attractive arena for quantum transport and spintronic phenomena based on the intriguing 2D metallic surface state.

Methods

Film preparation. $\text{Co}_3\text{Sn}_2\text{S}_2$ thin films were prepared by radio-frequency sputtering. The growth procedure is following and detail information can be found in previous studies^{24,25}. Firstly, a $\text{Co}_3\text{Sn}_2\text{S}_2$ film was deposited on Al_2O_3 (0001) substrate at 400 °C. Then, a SiO_x capping layer was deposited on the $\text{Co}_3\text{Sn}_2\text{S}_2$ film. The film was annealed at 800 °C in vacuum for 1 h. The crystal structures and composition were characterized by x-ray diffraction and energy-dispersive x-ray spectroscopy. The t (23–61 nm) was controlled by the deposition duration, which was confirmed by the Laue fringe in x-ray diffraction patterns.

Electrical transport measurement. Electrical measurements were carried out in physical property measurement system (PPMS, Quantum Design)²⁵. The films were scratched to make Hall-bar shape with indium contact electrodes. In the previous studies, the large anomalous Hall conductivity was observed in all films, indicating that the WSM phase is materialized.

Data availability

The data that support the findings of this study are available from the corresponding author upon reasonable request.

Received: 18 December 2020; Accepted: 14 May 2021;

Published online: 03 June 2021

References

- Ohtomo, A. & Hwang, H. Y. A high-mobility electron gas at the $\text{LaAlO}_3/\text{SrTiO}_3$ heterointerface. *Nature* **427**, 423–426 (2004).
- Chen, W., Chen, S., Qi, D. C., D., Gao, X. Y. & Wee, A. T. S. Surface transfer p-type doping of epitaxial graphene. *J. Am. Chem. Soc.* **129**, 10418–10422 (2007).
- Chua, L.-L. et al. General observation of n-type field-effect behaviour in organic semiconductors. *Nature* **434**, 194–199 (2005).
- Olsson, L. Ö. et al. Charge accumulation at InAs surfaces. *Phys. Rev. Lett.* **76**, 3626–3629 (1996).
- Ambacher, O. et al. Two dimensional electron gases induced by spontaneous and piezoelectric polarization in undoped and doped $\text{AlGaIn}/\text{GaIn}$ heterostructures. *J. Appl. Phys.* **87**, 334–344 (2000).
- Hasan, M. Z. & Kane, C. L. Colloquium: Topological insulators. *Rev. Mod. Phys.* **82**, 3045–3067 (2010).
- Yan, B. & Felser, C. Topological materials: Weyl semimetals. *Annu. Rev. Condens. Matter Phys.* **8**, 337–354 (2017).
- Armitage, N. P., Mele, E. J. & Vishwanath, A. Weyl and Dirac semimetals in three-dimensional solids. *Rev. Mod. Phys.* **90**, 015001 (2018).
- Mellnik, A. R. et al. Spin-transfer torque generated by a topological insulator. *Nature* **511**, 449–451 (2014).
- Soumyanarayanan, A., Reyren, N., Fert, A. & Panagopoulos, C. Emergent phenomena induced by spin-orbit coupling at surfaces and interfaces. *Nature* **539**, 509–517 (2016).
- Chang, C.-Z. et al. Experimental observation of the quantum anomalous Hall effect in a magnetic topological insulator. *Science* **340**, 167–170 (2013).
- Tokura, Y., Yasuda, K. & Tsukazaki, A. Magnetic topological insulators. *Nat. Rev. Phys.* **1**, 126–143 (2019).
- Potter, A. C., Kimchi, I. & Vishwanath, A. Quantum oscillations from surface Fermi arcs in Weyl and Dirac semimetals. *Nat. Commun.* **5**, 5161 (2014).
- Moll, P. J. W. et al. Transport evidence for Fermi-arc-mediated chirality transfer in the Dirac semimetal Cd_3As_2 . *Nature* **535**, 266–270 (2016).
- Zhang, Y. et al. Crossover of the three-dimensional topological insulator Bi_2Se_3 to the two-dimensional limit. *Nat. Phys.* **6**, 584–588 (2010).
- Li, Y.-Y. et al. Intrinsic topological insulator Bi_2Te_3 thin films on Si and their thickness limit. *Adv. Mater.* **22**, 4002–4007 (2010).
- Zhang, W., Yu, R., Zhang, H.-J., Dai, X. & Fang, Z. First-principles studies of the three-dimensional strong topological insulators Bi_2Te_3 , Bi_2Se_3 and Sb_2Te_3 . *New J. Phys.* **12**, 065013 (2010).
- Liu, E. et al. Giant anomalous Hall effect in a ferromagnetic kagome-lattice semimetal. *Nat. Phys.* **14**, 1125–1131 (2018).
- Wang, Q. et al. Large intrinsic anomalous Hall effect in half-metallic ferromagnet $\text{Co}_3\text{Sn}_2\text{S}_2$ with magnetic Weyl fermions. *Nat. Commun.* **9**, 3681 (2018).
- Li, G. et al. Surface states in bulk single crystal of topological semimetal $\text{Co}_3\text{Sn}_2\text{S}_2$ toward water oxidation. *Sci. Adv.* **5**, eaaw9867 (2019).
- Jiao, L. et al. Signatures for half-metallicity and nontrivial surface states in the kagome lattice Weyl semimetal $\text{Co}_3\text{Sn}_2\text{S}_2$. *Phys. Rev. B.* **99**, 245158 (2019).
- Morali, N. et al. Fermi-arc diversity on surface terminations of the magnetic Weyl semimetal $\text{Co}_3\text{Sn}_2\text{S}_2$. *Science* **365**, 1286–1291 (2019).
- Liu, D. F. et al. Magnetic Weyl semimetal phase in a Kagomé crystal. *Science* **365**, 1282–1285 (2019).
- Fujiwara, K. et al. Ferromagnetic $\text{Co}_3\text{Sn}_2\text{S}_2$ thin films fabricated by co-sputtering. *Jpn. J. Appl. Phys.* **58**, 050912 (2019).
- Ikeda, J. et al. Critical thickness for the emergence of Weyl features in $\text{Co}_3\text{Sn}_2\text{S}_2$ thin films. *Commun. Mater.* **2**, 18 (2021).
- Ozawa, A. & Nomura, K. Two-orbital effective model for magnetic Weyl semimetal in Kagome-lattice shandite. *J. Phys. Soc. Jpn* **88**, 123703 (2019).
- Goodings, D. A. Electrical resistivity of ferromagnetic metals at low temperatures. *Phys. Rev.* **132**, 542–558 (1963).
- Furukawa, N. Unconventional one-magnon scattering resistivity in half-metals. *J. Phys. Soc. Jpn.* **69**, 1954–1957 (2000).
- Bombor, D. et al. Half-metallic ferromagnetism in the Heusler compound Co_2FeSi . *Phys. Rev. Lett.* **110**, 066601 (2013).
- Muechler, L. et al. Emerging chiral edge states from the confinement of a magnetic Weyl semimetal in $\text{Co}_3\text{Sn}_2\text{S}_2$. *Phys. Rev. B.* **101**, 115106 (2020).
- Xu, Q. et al. Topological surface Fermi arcs in the magnetic Weyl semimetal $\text{Co}_3\text{Sn}_2\text{S}_2$. *Phys. Rev. B.* **97**, 235416 (2018).
- Xing, Y. et al. Localized spin-orbit polaron in magnetic Weyl semimetal $\text{Co}_3\text{Sn}_2\text{S}_2$. *Nat. Commun.* **11**, 5613 (2020).

Acknowledgements

The authors are grateful to S. Ito and M. Nagasako for the transmission electron microscopy analysis and K. Kobayashi, Y. Yanagi, M.-T. Suzuki, and Y. Motome for fruitful discussions. This work was performed under the Inter-University Cooperative Research Program of the Institute for Materials Research, Tohoku University (Proposal No. 19G0410). This work was supported by JSPS KAKENHI (Grant No. 20H01830) and JST CREST (JPMJCR18T2).

Author contributions

J.I. and K.F. grew the films and measured the electrical transport properties. J.S. performed the magnetoresistance measurements. K.F. performed the magnetization measurements under the support by J.S., T.S., and K.T.; J.I. and K.F. analyzed the measured data. K.N. contributed to theoretical interpretations of the experimental results. J.I., K.F., and A.T. wrote the manuscript with input from other authors. All authors discussed the results. A.T. supervised the project.

Competing interests

The authors declare no competing interests.

Additional information

Supplementary information The online version contains supplementary material available at <https://doi.org/10.1038/s42005-021-00627-y>.

Correspondence and requests for materials should be addressed to K.F.

Peer review information *Communications Physics* thanks the anonymous reviewers for their contribution to the peer review of this work. Peer reviewer reports are available.

Reprints and permission information is available at <http://www.nature.com/reprints>

Publisher's note Springer Nature remains neutral with regard to jurisdictional claims in published maps and institutional affiliations.



Open Access This article is licensed under a Creative Commons Attribution 4.0 International License, which permits use, sharing, adaptation, distribution and reproduction in any medium or format, as long as you give appropriate credit to the original author(s) and the source, provide a link to the Creative Commons license, and indicate if changes were made. The images or other third party material in this article are included in the article's Creative Commons license, unless indicated otherwise in a credit line to the material. If material is not included in the article's Creative Commons license and your intended use is not permitted by statutory regulation or exceeds the permitted use, you will need to obtain permission directly from the copyright holder. To view a copy of this license, visit <http://creativecommons.org/licenses/by/4.0/>.

© The Author(s) 2021